

## Determination of the shape and size of aggregated phases in $\text{NaCl:Mn}^{2+}$ by small-angle neutron scattering

F. Rodríguez, J. C. Gómez Sal, and M. Moreno

*DCITYM, Facultad de Ciencias, Universidad de Cantabria, 39005 Santander, Spain*

A. de Geyer and C. Janot

*Institut Max von Laue—Paul Langevin (ILL), Centre de Tri, avenue des Martyrs, Boîte Postale No. 156X, 38042 Grenoble CEDEX, France*

(Received 9 August 1990)

Suzuki-phase precipitates formed in  $\text{NaCl:Mn}^{2+}$  have been studied by small-angle neutron scattering. The experiments, carried out on single crystals of NaCl with different  $\text{Mn}^{2+}$  concentrations, indicate the usefulness of this technique for detecting precipitates and for determining their shape and size. A salient feature of the present work is the anisotropic character of the neutron-scattering intensity, which provides a way for determining the size of the precipitate out of the Guinier region. The analysis of the intensity decay allows us to detect precipitate shapes displaying slight modifications with respect to the perfect cube.

### INTRODUCTION

Certain properties of materials are greatly influenced by the presence of impurities and sometimes also by their aggregation state. In alkali halides doped with transition-metal ions, the presence of aggregated phases with well-defined crystalline structures has often been observed.<sup>1-10</sup> In particular, as-grown  $\text{Mn}^{2+}$ -doped NaCl crystals usually contain Suzuki-phase (SP) microcrystals, even for a  $\text{Mn}^{2+}$  concentration of about 100 ppm. This phase of the formula  $\text{Na}_6\text{MnCl}_8$  belongs to the  $Fm\bar{3}m$  space group with a lattice parameter twice that of the NaCl cell. The crystallographic axes of the cubic SP coincide with those of the NaCl crystal, as has been shown by x-ray diffraction<sup>7</sup> and Raman techniques.<sup>11</sup> The SP precipitates have also been widely studied by means of different techniques: photoluminescence,<sup>12</sup> electron paramagnetic resonance (EPR),<sup>13</sup> magnetization,<sup>14</sup> and specific-heat measurements.<sup>15</sup> The optical, magnetic, and thermal properties of this phase differ markedly from those of the same crystal having the  $\text{Mn}^{2+}$  ions as isolated impurities. Furthermore, precipitates are very useful systems for studying size effects. The influence of precipitate size on the magnetic properties of the SP has recently been evidenced through magnetic measurements carried out in the very-low- (0.07–1-K) temperature range.<sup>14</sup> Magnetic and specific-heat measurements have evidenced that the SP aggregates become antiferromagnetic below  $T_N=0.2$  K. Besides the antiferromagnetic contribution, an anomalous superimposed susceptibility depending on  $\text{Mn}^{2+}$  concentration was observed. This behavior was explained in terms of precipitate size, which should be about 1000 Å for the systems under study.

The aim of this work is to investigate, by small-angle neutron scattering (SANS), the existence, shape, and size of these precipitates in  $\text{NaCl:Mn}^{2+}$  single crystals. A salient feature of the present work is that information

about sizes of precipitates is obtained using SANS, but in the region in which the Guinier law does not hold. In fact, since the smallest  $q$  scattering vector available in these experiments is  $10^{-3} \text{ Å}^{-1}$ , only precipitates having a size smaller than  $\sim 500 \text{ Å}$  can be determined through the standard method using the Guinier law. It is also shown that SANS allows us to detect precipitate shapes displaying slight differences from a pure cube. The advantages of SANS with respect to other techniques are the following: (a) The Suzuki phase provides larger contrast for neutrons ( $b_{\text{Mn}}=-0.373, b_{\text{Na}}=0.363 \times 10^{-12} \text{ cm}$ ) than for x-ray and light scattering. (b) In contrast to small-angle light scattering, SANS allows one to determine sizes down to 10 Å. (c) SANS is a nondestructive technique in contrast to electron-microscopy techniques and x-ray scattering where radiation-induced damage is unavoidable for these materials. The usefulness of SANS for exploring precipitate formation in these materials has been successfully tested previously.<sup>16</sup>

### EXPERIMENT

$\text{NaCl:Mn}^{2+}$  single crystals were grown by the Czochralski method in an argon atmosphere, employing Merck Suprapur base compounds in the Laboratorio de Crecimiento Cristalino at the Universidad Autónoma de Madrid. Cleavage samples in the (100) plane of about  $10 \times 10 \times 2 \text{ mm}^3$  with different  $\text{Mn}^{2+}$  concentrations were used in these experiments: 5.000 ppm (sample A), 3.300 ppm (sample B), 1.300 ppm (sample C), and pure NaCl crystals (sample D). These concentrations were determined by atomic absorption spectroscopy and the presence of Suzuki-phase precipitates evidenced by optical and EPR techniques. The influence of thermal treatment was also analyzed in two samples of type (B): one sample ( $B_a$ ) was annealed at 250 °C for 2 h while the other one ( $B_q$ ) was quenched from 550 °C to room temperature on a copper block.

SANS experiments were carried out on the D11 instrument at the I.L.L. (Grenoble) under the following experimental conditions: neutron wavelength  $\lambda = 10.25$  Å, sample-detector distances 20 and 35 m, and scattering-vector range ( $q = K - K_0$ ),  $10^{-3} < q < 10^{-2}$  Å<sup>-1</sup>. Experiments were performed at room temperature. The intensities of the scattered neutrons have been corrected using pure NaCl single crystals as a reference.

## RESULTS

Figure 1 shows the two-dimensional contour intensity plots of NaCl:Mn<sup>2+</sup> samples *A*, *B*, and *C*. These contours were not observed in the pure NaCl sample *D*: Only a flat background was detected in this sample. It is worth noting the anisotropic character of these contours revealing fourfold symmetry. Within the same  $q$  range, these starlike patterns become sharper as the Mn<sup>2+</sup> concentration increases. The dependence of the corrected intensities along the [100] direction in  $q$  space is presented in Fig. 2 for different Mn<sup>2+</sup> concentrations. From inspection of both Figs. 1 and 2, two facts come out: (1) The scattered neutron intensity increases with Mn<sup>2+</sup> concentration, and (2) the decay behavior of  $I(q)$  depends on the  $q$  direction, with [100] and [110] being the extreme cases. In no case is a linear dependence of  $\ln I(q)$  versus  $q^2$  (Guinier plot) observed along any direction. However, a clear linear behavior is seen in the  $\ln I(q)$  versus  $\ln q$  representation, as is shown in the insert of Fig. 2 and in Fig. 3. A dependence  $I(q) \propto q^{-n}$  with  $n=2.5$  for [100]

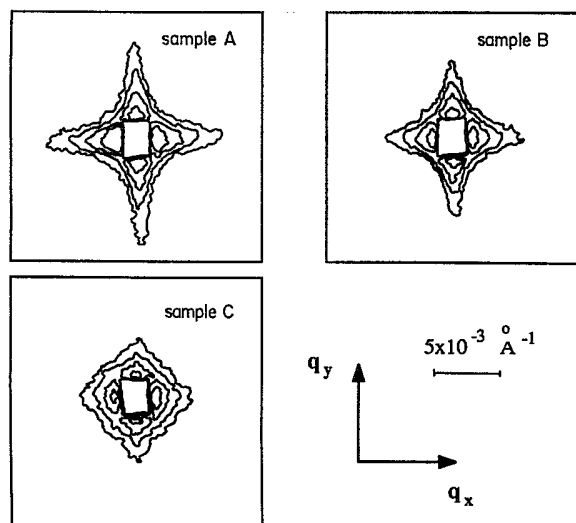


FIG. 1. SANS intensity contour plots,  $I(q) = \text{const}$ , for NaCl:Mn<sup>2+</sup> samples *A*, *B*, and *C*. The incoming neutron beam is directed along the [001] crystal axis ( $z$  direction). The [100] and [010] crystallographic directions ( $x$  and  $y$  directions, respectively) are oriented parallel to the multidetector. The external contours correspond to relative intensities  $I(q_x, q_y) = 100$  for samples *A* and *B*, and 50 for sample *C*. The intensity doubles in value for successive internal contours. The rectangle at the center represents the beam stop. Uncorrected data.

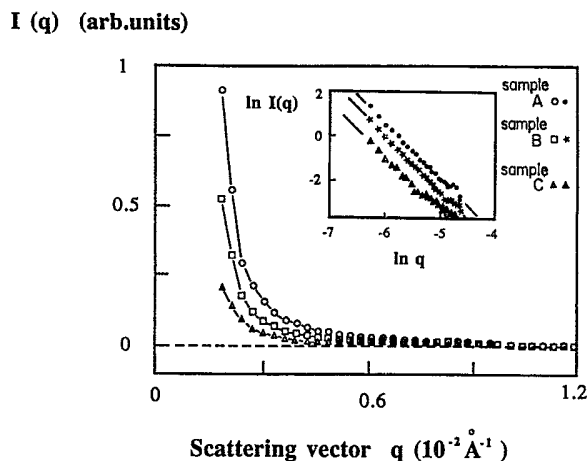


FIG. 2. Intensity dependence on the scattering wave vector  $q$  along the [100] direction, for samples *A*, *B*, and *C*. Intensities are corrected for sample transmission and detector efficiency using the pure NaCl intensity as background reference. The inset shows the logarithmic representation  $\ln I(q)$  vs  $\ln q$  along the [100]  $q$  direction. Straight lines with  $-2.5$  slopes are drawn through the experimental points.

direction and  $n=3.5$  for [110], appears in all the samples studied of types *A*, *B*, and *C*.

The thermal treatments of annealing and quenching carried out on sample *B* have different effects on both the intensity contours and  $q$  dependence. While the annealed sample ( $B_a$ ) displays the same contour plot as *B*, the contour plot corresponding to the quenched one ( $B_q$ ) is clearly modified. The contour pattern becomes isotropic and the intensity is strongly reduced for low  $q$ , showing a maximum at  $q = 4 \times 10^{-3}$  Å<sup>-1</sup> (Fig. 4). For  $q$  values greater than  $5 \times 10^{-3}$  Å<sup>-1</sup>, the intensity of  $B_q$  is higher than that of sample *B*.

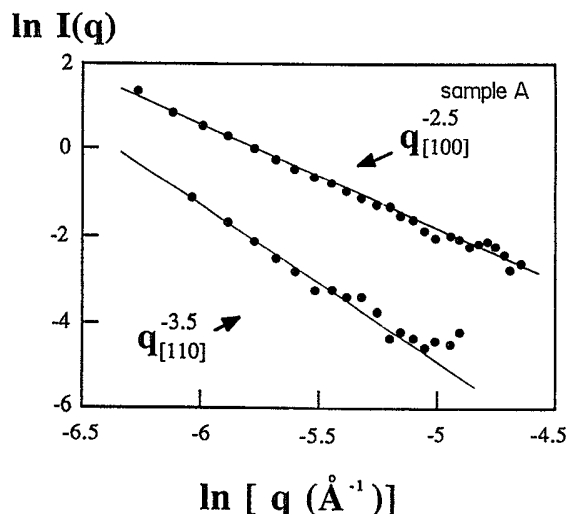


FIG. 3.  $\ln I(q)$  vs  $\ln q$  representation for sample *A* along the [100] and [110]  $q$  directions. Linear dependences with slopes of  $-2.5$  and  $-3.5$ , respectively, are found in these directions.

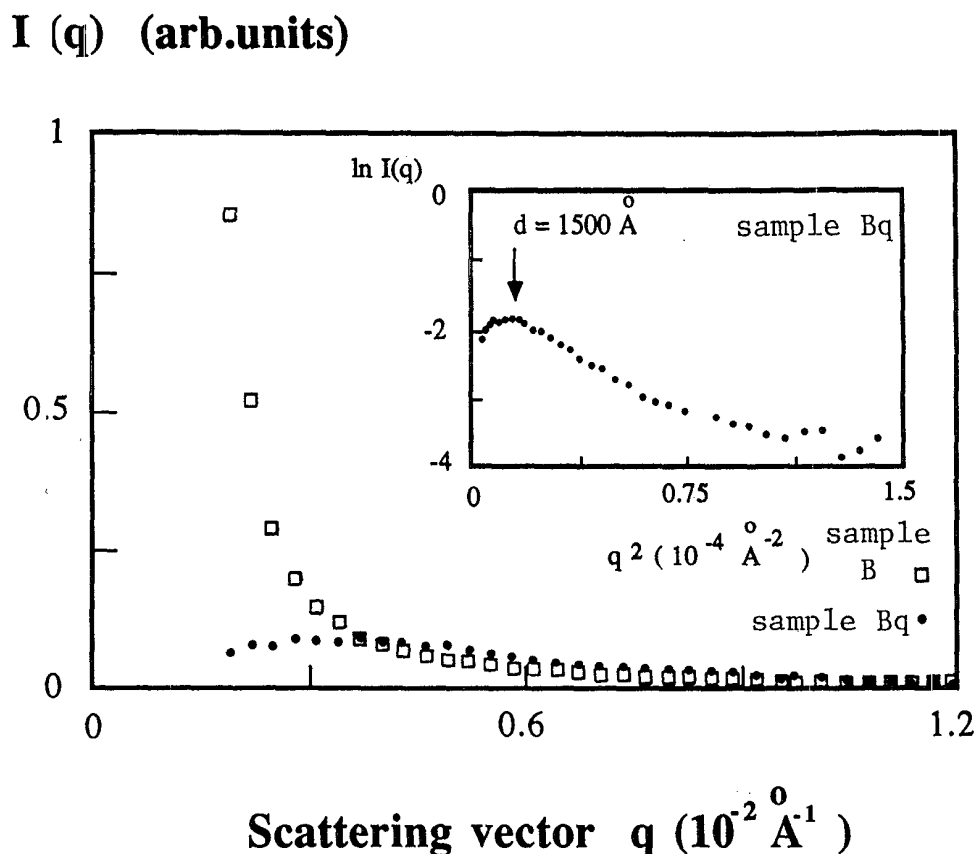


FIG. 4. Variation of the SANS intensity  $I(q)$  upon thermal quenching of sample B.  $q$  is taken along [100] for sample B and its modulus for  $B_q$  (isotropic contour). The inset displays a magnification of the intensity for sample  $B_q$  using a  $\ln I(q)$  vs  $q^2$  representation.

## ANALYSIS AND DISCUSSION

The strong correlation between the  $\text{Mn}^{2+}$  concentration and the corrected scattered intensity displayed in Fig. 2 clearly indicates that SANS is due to the presence of  $\text{Mn}^{2+}$ . Therefore, the contour plots of Fig. 1 are completely associated with the SP microcrystals in  $\text{NaCl}:\text{Mn}^{2+}$ .

In this situation the small-angle scattered intensity  $I(q)$  due to the presence of precipitates is proportional to the scattering cross section  $d\sigma(q)/d\Omega$ , which is directly related to the distribution, shape and size of the precipitates.<sup>17</sup> In the case of identical particles,

$$d\sigma(q)/d\Omega = \Phi S(q) |F(q)|^2. \quad (1)$$

$\Phi = N/V$  is the density of particles,  $S(q)$  is the interference function due to correlations between particles, and  $F(q)$  is the form factor of the particle defined as

$$F(q) = \int_V [\rho(\mathbf{R}) - \rho_0] \exp(i\mathbf{q} \cdot \mathbf{R}) d^3\mathbf{R}. \quad (2)$$

The integral extends over the whole particle volume  $V_p$ ,  $\rho$  and  $\rho_0$  are the locally averaged scattering length densities for the particle and host matrix, respectively, which are constant for homogeneous particles.<sup>17</sup> In dilute systems, where  $L \gg 2\pi/q_{\min}$  ( $L$  being the mean in-

terparticle distance and  $q_{\min}$  the smallest scattering vector available in the experiment),  $S(q) = 1$ . It follows directly that the scattering cross section  $d\sigma(q)/d\Omega$  is the squared modulus of the Fourier transform of the particle shape. Assuming that the present case is a dilute system, as will be justified later, the form of the bidimensional contour plots of Fig. 1 directly reflects the symmetry of the precipitate. These contours clearly indicate that the SP precipitates are not isotropic (spheres), but display the same cubic symmetry as the host NaCl crystal, along the  $z$  direction of the incoming neutron beam ([001] direction).

In order to obtain more insight into the shape and size of the SP microcrystals, it is necessary to propose an adequate model which can explain our experimental results.

The simplest particle model which can account for the starlike contour form is a cube with (100)-type faces parallel to the corresponding ones in NaCl. The form factor of a cube with an edge length  $a_0$  is given by

$$F(q) = F(Q) = V (\sin Q_x \sin Q_y \sin Q_z / Q_x Q_y Q_z), \quad (3)$$

with  $Q_i = q_i a$ ,  $a = a_0/2$ ,  $i = x, y, z$ , and  $V = a_0^3$  is the cube volume.

In our experiments with incoming neutrons along the  $z$  direction, i.e.,  $q_z \approx 0$ , the contour plots defined in the

( $q_x, q_y$ ) plane are roughly explained by the form factor given in Eq. (3). The fact that no maximum is observed in the  $I(q)$  curves, as expected from  $|F(q)|^2$ , is mainly attributed to the different sizes of SP precipitates in our samples (polydispersity) as well as to the  $q$  resolution of the multidetector ( $1 \times 1 \text{ cm}^2$  element size) and the wavelength resolution (9%).

An outstanding point concerning these anisotropic precipitates is the possibility of determining their mean size outside of the Guinier approximation even without knowing the extrapolated  $I(q)$  values at  $q=0$ . This is the present case, where the experimental results in Figs. 1–3 show that  $Q > 1$  and thus we are not in the Guinier region corresponding to  $Q \ll 1$ . In fact, for the limit  $Q \ll 1$ ,  $I(q) \propto 1 - (\alpha^2/3)|q|^2$  leading to a linear  $q^2$  dependence:  $\ln I(q) \propto (\alpha^2/3)q^2$ . This expression is similar to that obtained in the case of spheres substituting  $\alpha$  for  $R_G$  (gyration radius). In this region a direct estimation of  $\alpha$  can be derived from the slope of the Guinier plot, and also isotropic contour plots should be expected for the cube in this limit. This is obviously not the present case in view of the experimental results given above. Assuming  $Q = qa > 1$  and given size distribution of cubes in our system, the intensity  $I(Q)$ , averaged over the different particles, leads to

$$\begin{aligned} I(Q^{[100]}) &\propto \langle V^2(\sin^2 Q_x^{100}) / (Q_x^{100})^2 \rangle \\ &\propto \frac{1}{2} (1 / (Q_x^{[100]})^2), \\ I(Q^{[110]}) &\propto \langle V^2(\sin^4 Q_x^{110}) / (Q_x^{110})^4 \rangle \\ &\propto \frac{3}{8} (1 / (Q_x^{[110]})^4), \end{aligned} \quad (4)$$

where  $V = 8\alpha^3$  and  $Q_x^{[hk0]}$  is the  $x$  component of  $Q$  along the  $[hk0]$  direction. These intensity dependences give rise to the same contour plots presented in Fig. 1. The starlike form becomes sharper for higher  $Q$  values, that is to say, for higher particle sizes. Furthermore, it is possible to obtain a first estimation of the cube size  $\alpha$  from these figures from the ratio  $I_{[100]}/I_{[110]}$  for any value of  $|q|$ . From Eqs. (4),  $\alpha$  is given by

$$\alpha = \sqrt{3}/2q_x^{[100]} / (q_x^{[110]})^2 (I_{[100]}/I_{[110]})^{1/2}, \quad (5)$$

where  $I_{[100]} = I(q_x^{[100]})$  and  $I_{[110]} = I(q_x^{[110]})$ .

By taking only one of the intensity contours,  $I(q) = \text{const}$ , where  $I_{[100]}/I_{[110]} = 1$ , the particle size  $\alpha$  is easily calculated through the maximum  $q_x^{[100]}$  and minimum  $Q_x^{[110]}$  experimental values of the contour by  $\alpha = \sqrt{3}/2q_x^{[100]} / (q_x^{[110]})^2$ . The mean values of the cube edge  $a_0 = 2\alpha$  of SP precipitates deduced in this manner are 2700, 2000, and 1400 Å for samples A, B, and C, respectively (Table I). An important conclusion is that larger particle sizes correspond to higher  $\text{Mn}^{2+}$  concentrations. However, this model fails when this estimation is extended to other intensity contours, and in particular, different sizes are derived for the same sample using the contours taken at a detector distance of 35 m. This fact is evidenced in Fig. 3, which shows an intensity  $q$  dependence of  $q^{-2.5}$  along  $[100]$  and  $q^{-3.5}$  along  $[110]$  instead of the  $-2$  and  $-4$  exponents characteristic of perfect cubes. In order to obtain reliable values of  $\alpha$  from the intensity contour plots according to the real variations of  $I(q)$ , it would be necessary to know the scale factor  $C$ , connecting  $Q^{[100]}$  and  $Q^{[110]}$  within the same contour:  $(Q_x^{[100]})^{-2.5} / (Q_x^{[110]})^{-3.5} = C$ . In perfect cubes with dependences of  $[Q_x^{[100]}]^{-2}$  and  $[Q_x^{[110]}]^{-4}$ , the scale factor  $C$  is  $\frac{3}{4}$ .

At this stage of the analysis, it is worthwhile to investigate whether slight modifications of the cube, leading to other cubic forms, could give rise to  $q$  dependences in the scattering intensity with nonintegral exponents in the framework of our independent-particle model [ $S(q) = 1$ ]. In this sense cube deformations tending to smooth off the edges and corners of the cube might lead to intensity variations  $I(q)$ , which would correspond neither to a cube nor a sphere with intensity varying with  $q^{-4}$ , but would preserve the cubic symmetry of the particle.

Before treating three-dimensional particle modifications, we have explored the simpler two-dimensional case of modified squares, in order to check the existence of linear  $\ln I$  versus  $\ln Q$  behavior with

TABLE I. Sizes  $a_0 = 2\alpha$  of the Suzuki-phase precipitates in  $\text{NaCl}:\text{Mn}^{2+}$  for different  $\text{Mn}^{2+}$  concentrations. The sizes are given for two types of particle: perfect cube and deformed cube. In the first model the value of  $a_0$  has been deduced for the contour with  $q_{[110]} = 3 \times 10^{-3} \text{ Å}^{-1}$  and  $\Delta a_0$  represents the difference of sizes  $a_0$ , calculated with the contours corresponding to  $q_{[110]} = 2 \times 10^{-3}$  and  $5 \times 10^{-3} \text{ Å}^{-1}$ , respectively. The sizes  $a_0$  in the deformed cube model have been obtained by using a scale factor  $C = \frac{1}{6}$  characteristic of a monodisperse system of particles with  $N = 50$ ,  $N_t = 10$ , and  $\beta = 0.45$ . The table includes the ratio of  $\text{Mn}^{2+}$  on surface to  $\text{Mn}^{2+}$  in bulk.

$\text{NaCl}:\text{Mn}^{2+}$ sample	A	B	C
$\text{Mn}^{2+}$ Concentration (ppm)	5000	3300	1300
$a_0$ (Å) Perfect cube	2700	2000	1400
$\Delta a_0$ (Å)	1000	800	500
$a_0$ (Å) Deformed cube	3000	1600	700
$\text{Mn}^{2+}$ on surface (%)	1	2	5
$\text{Mn}^{2+}$ in bulk			

nonintegral exponents along the [10] and [11] directions in  $q$  space.

Figure 5 portrays the two squares ( $\{10\}$  forms) with  $\{11\}$  form modification (case  $a$ ) and the simple  $\{hk\}$  form (case  $b$ ), respectively. Intensity calculations as a function of the parameter  $\beta$ , defined in Fig. 5, indicate that there is a linear dependence of  $\ln I$  versus  $\ln Q$  with nonintegral exponents for a wide range of  $\beta$ . The exponent  $n$  along [10] and [11] varies with  $\beta$  as depicted in Fig. 5. For the extreme cases  $\beta=0$  and 1, the values of  $n$  change from 2 and 4 to 4 and 2, respectively, as expected for two squares rotated  $45^\circ$ . In any case, small changes in  $\beta$  give rise to nonintegral  $n$  values less than 4 and greater than 2, respectively. In case  $a$  both exponents are close to 2.3 for  $\beta=0.59$ , which represents the octagon. Except for the perfect square, the present bidimensional results cannot be extrapolated to the real cubic three-dimensional case because they would represent particles with tetragonal symmetry. However, these results clearly suggest that it would be possible to reproduce the experimental values with an adequate three-dimensional particle model.

Two models of cubic particles have been worked out: (a) a cube with rhombododecahedral deformation ( $\{100\} + \{111\}$  forms) and (b) a cube with tetrahexahedral deformation ( $\{100\} + \{hk0\}$  forms). The scattered intensity was calculated for both a monodisperse system and a Gaussian distribution of particle size (polydispersity), maintaining the same shape of the particle. The form factor  $F(Q)$  was determined for different degrees of particle deformation. Details of the calculation of  $F(Q)$  are given in the Appendix.

The first model cannot explain the observed intensity decays  $I(q)$  because it leads to small variations along the [100] direction. But the second one, illustrated in Fig. 6, gives the desired results. The linear dependence of  $\ln I$  versus  $\ln Q$  is presented in Fig. 7 for three different particle shapes. The exponents  $n$  ( $I \propto Q^{-n}$ ) were obtained by

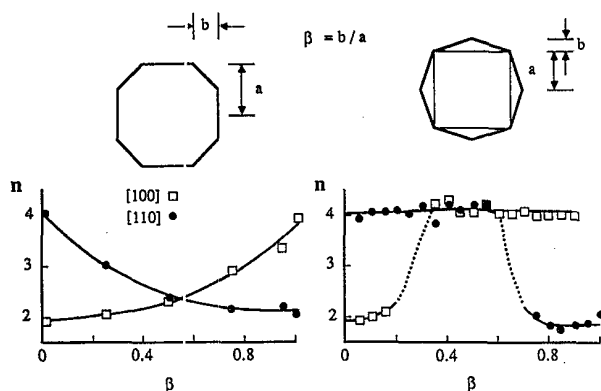


FIG. 5. Variation of the exponent  $n$  relating the intensity  $Q$  dependence,  $I(Q) \propto Q^{-n}$  ( $Q = qa$ ), with the parameter  $\beta$ , for the two square forms given at the top of the figure. The values of  $n$  are calculated for the [10] and [11]  $Q$  directions. The dotted lines in the square form  $\{hk\}$  indicate that nonlinear dependence  $\ln I$  vs  $\ln Q$  has been found in this interval of  $\beta$ .

a least-squares fitting in the range  $1 < \ln Q < 4$ ; they are also represented in Fig. 7 as a function of  $\beta$  and  $N_t$ . Our experimental results are well reproduced for  $\beta=0.45$ ,  $N_t=10$ , and  $N=50$ , leading to a scale factor  $C = \frac{1}{6}$  so that, for one intensity contour,

$$(Q_x^{[100]})^{-2.5} / (Q_x^{[110]})^{-3.5} = \frac{1}{6}, \quad (6)$$

$$a = \frac{1}{6} (q_x^{[100]})^{2.5} / [q_x^{[110]}]^{3.5}.$$

Since the same exponents ( $-2.5$  and  $-3.5$ ) have been observed within the experimental accuracy for samples  $A$ ,  $B$ , and  $C$ , it is assumed that their particle shape and, therefore, the scale factor are the same. The sizes of the SP precipitates have been obtained over the whole  $q$  range studied using Eq. (6), and they are given in Table I. It is worth mentioning that these values obtained with the adequate scale factors do not differ very much from those estimated assuming perfect cube shapes, though small deformations lead to notable changes in the decay of  $I(q)$ .

Another interesting result concerns the influence of thermal treatments on the shape and size of the SP precipitates presented in Fig. 4. In contrast to annealing, quenching tends to dilute the  $Mn^{2+}$  ions initially aggregated as SP in the NaCl crystal. The SANS technique has been especially useful for studying this phenomenon.

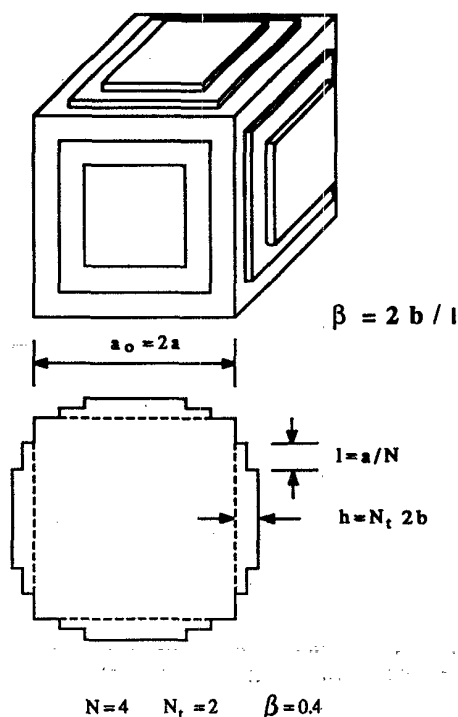


FIG. 6. Three-dimensional cubic form  $\{100\} + \{hk0\}$ . This form is generated from a perfect cube by adding  $N_t$  parallelepiped steps of height  $2b$ ; interstep distance is  $l = a/N_t$ , where  $a$  is the cube semiedge. The parameter  $\beta$  is defined as  $\beta = 2b/l = h/aN_t/N_t$ .

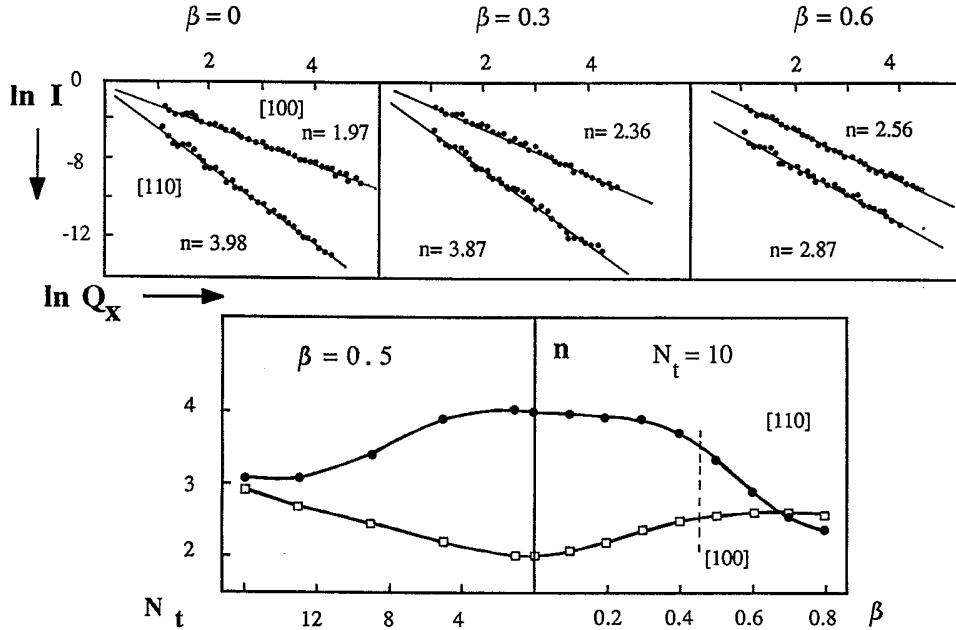


FIG. 7. Calculated values of the SANS intensity  $I(Q_x)$  with  $Q_x = q_x \alpha$  along the [100] and [110] Q directions for the cubic form given in Fig. 6. The three figures at the top show  $\ln I(Q_x)$  vs  $\ln Q_x$  representations, using  $N = 50$ ,  $N_t = 10$ , and  $\beta = 0, 0.3$ , and  $0.6$ , respectively. Black dots represent the simulated values, and straight lines are the least-squares fit within the interval  $1 < \ln Q < 4$  interval. The figure below represents the variation of the exponent  $n$  with  $\beta$  (right side) and  $N_t$  (left side) for  $N_t = 10$  and  $\beta = 0.5$ , respectively.  $N = 50$  in both cases. The dotted line at  $\beta = 0.45$  indicates the best fit to the experimental values of 2.5 and 3.5 for the [100] and [110] Q directions, respectively.

Both the intensity contours and the  $I(q)$  curves (Fig. 4) differ substantially for the samples  $B$  and  $B_q$ . The cubic contours of  $B$  become isotropic for  $B_q$ , indicating that precipitates are still present in this sample after quenching, but have different shapes and sizes. Even in the simplest case of spherical particles, the occurrence of a maximum in the  $I(q)$  curve for  $B_q$  clearly indicates particle correlations:  $S(q) \neq 1$ . A mean interparticle distance  $d \approx 1500 \text{ \AA}$  is derived with  $d \approx 2\pi/q_{\max}$ . This correlation distance can be explained by the decrease in the precipitate size and thus an increase in the number of precipitates. For samples  $A$ ,  $B$ , and  $C$ , without thermal treatments, a rough estimation of the interparticle distance  $d$  can be made knowing the precipitate sizes and the  $\text{Mn}^{2+}$  concentration. Distances much greater than  $3000 \text{ \AA}$  are obtained from the values of  $\alpha$  given in Table I, and thus the independent particle assumption employed in our model is well justified.

As a final remark, we wish to point out that the present results confirm the interpretation given in Ref. 14 to explain the magnetic behavior of the SP. This interpretation was based on the assumption that the size of precipitate increases with increasing  $\text{Mn}^{2+}$  concentration, which is clearly demonstrated in the present work. In particular, the view that the anomalous magnetic contribution can be related to surface effects is corroborated by comparing the ratios of  $\text{Mn}^{2+}$  on the surface to  $\text{Mn}^{2+}$  inside the precipitate (Table I) obtained in this work and from the magnetic measurements of Ref. 14.

#### ACKNOWLEDGMENTS

This work has been supported by the CICYT.

#### APPENDIX

The calculation of the SANS intensity due to a monodisperse system of homogeneous particles involves the Fourier transform (FT) given by

$$\mathcal{F}(\mathbf{Q}) = \int_{\text{vol}} |\rho(\mathbf{R}) - \rho_0| e^{-i\mathbf{Q} \cdot \mathbf{R}} d^3\mathbf{R}. \quad (\text{A1})$$

Assuming a constant value of the contrast within the particle,  $\rho(\mathbf{R}) - \rho_0$ , this integral becomes very simple in the case of parallelepiped particles:

$$\mathcal{F}(\mathbf{Q}) = V \frac{\sin Q_x \alpha_x}{Q_x} \frac{\sin Q_y \alpha_y}{Q_y} \frac{\sin Q_z \alpha_z}{Q_z}, \quad (\text{A2})$$

with  $Q_i = q_i \alpha_i$ ,  $i = x, y, z$ ,  $\alpha_i = a, b, c$  the semiedges of the parallelepiped, and  $V$  is the particle volume,  $V = 8abc$ . In the present case of particles with  $\{100\} + \{hk0\}$  forms (Fig. 6), we have built up the  $\{hk0\}$  form by using parallelepipeds of height  $h = 2\ell$  and square base of semiedge  $a - L$ ,  $L$ , decreasing with the number of steps,  $n$ , as  $L = an/N$ . Though this form leads to flat  $\{hk0\}$  faces in the limit  $N \rightarrow \infty$ , a more realistic description of this precipitate is obtained by using steps when the mean size of the precipitate is about  $10^3 \text{ \AA}$ .

The FT of a given particle defined with the parameters  $N_t$  (number of steps),  $l = a/N$  (interstep distance), and  $2\ell$  (step height) becomes

$$\mathcal{F}(\mathbf{Q}) = \mathcal{F}^c(\mathbf{Q}) + \mathcal{F}'(\mathbf{Q}), \quad (\text{A3})$$

where  $\mathcal{F}^c(\mathbf{Q})$  is the FT of the perfect cube with edge  $a_0 = 2a$  and  $\mathcal{F}'(\mathbf{Q})$  is the contribution of all the steps.  $\mathcal{F}'(\mathbf{Q})$  can easily be evaluated by using the symmetry transformation of the particle. For a given direction  $OZ$ , the  $\mathcal{F}'_z(\mathbf{Q})$  becomes

$$\mathcal{F}'_z(\mathbf{Q}) = 8 \sum \exp\{iq_z[\alpha + (2n-1)\ell]\} \frac{\sin[q_x(\alpha - n\ell)]}{q_x} \frac{\sin[q_y(\alpha - n\ell)]}{q_y} \frac{\sin(q_z\ell)}{q_z}, \quad (\text{A4})$$

and the total FT,

$$\begin{aligned} \mathcal{F}'(\mathbf{Q}) = 16 \left\{ \frac{\sin q_z \ell}{q_x q_y q_z} \sum_{n=1}^{N_t} \cos\{[\alpha + (2n-1)\ell]q_z\} \sin[q_x(\alpha - n\ell)] \sin[q_y(\alpha - n\ell)] \right. \\ + \frac{\sin q_y \ell}{q_x q_y q_z} \sum_{n=1}^{N_t} \cos\{[\alpha + (2n-1)\ell]q_y\} \sin[q_x(\alpha - n\ell)] \sin[q_z(\alpha - n\ell)] \\ \left. + \frac{\sin q_x \ell}{q_x q_y q_z} \sum_{n=1}^{N_t} \cos\{[\alpha + (2n-1)\ell]q_x\} \sin[q_y(\alpha - n\ell)] \sin[q_z(\alpha - n\ell)] \right\}, \quad (\text{A5}) \end{aligned}$$

where the summations are from  $n=1$  to  $N_t$ .

We are interested in the limits  $q_y \rightarrow 0$  and  $q_y \rightarrow q_x$ , both with  $q_z \rightarrow 0$ , to explore the intensities along [100] and [110]  $q$  directions, respectively.

Expression (A5) becomes

$$\mathcal{F}'(\mathbf{Q}) = \frac{2V}{Q_x} \left[ \beta/N \sum_{n=1}^{N_t} (1-n/N) \sin\{Q_x(1-n/N)\} + \sin \left[ \frac{\beta Q_x}{2N} \right] \sum_{n=1}^{N_t} (1-n/N)^2 \cos\{Q_x[1+\beta(2n-1)/2N]\} \right], \quad (\text{A6})$$

for [100], and

$$\begin{aligned} \mathcal{F}'(\mathbf{Q}) = 2V/Q_x^2 \left[ \frac{\beta}{2N} \sum_{n=1}^{N_t} \sin^2\{Q_x(1-n/N)\} + 2 \sin \left[ \frac{\beta Q_x}{2N} \right] \sum_{n=1}^{N_t} (1-n/N) \cos\{Q_x[1+\beta(2n-1)/2N]\} \right. \\ \left. = \sin\{Q_x(1-n/N)\} \right], \quad (\text{A7}) \end{aligned}$$

for [110], where  $Q_x = q_x \alpha$  and  $\beta = 2\ell/l$ .

The total FT of the particle must also include the term  $\mathcal{F}^c(\mathbf{Q})$  of the perfect cube which is  $V \sin Q_x / Q_x$  and  $V \sin^2 Q_x / Q_x^2$ , along [100] and [110], respectively.

The intensity is simply proportional to the square modulus of the  $\mathcal{F}(\mathbf{Q})$ . This intensity shows oscillations because of the sine and cosine dependences. However, even in the case of monodisperse systems, such oscillations are modulated by the experimental  $q$  resolution. In the D11 instrument at ILL, the spatial resolution of the multidetector is  $1 \times 1 \text{ cm}^2$ , which corresponds to  $\Delta q = 3 \times 10^{-4} \text{ \AA}^{-1}$  for  $L = 20 \text{ m}$  and  $\lambda = 10.25 \text{ \AA}$  with  $\Delta\lambda = 1 \text{ \AA}$ . In our case the intensity  $I(\mathbf{Q}) = |\mathcal{F}(\mathbf{Q})|^2$  has been averaged over the  $Q_x$  interval  $\Delta Q_x = \pm 1$ . The values of the intensity  $I(\mathbf{Q})$  calculated following this procedure are represented in Fig. 7 with  $N = 50$ ,  $N_t = 10$  and  $\beta = 0, 0.3$ , and  $0.6$ . The values  $I(\mathbf{Q})$  represent  $\langle |V^{-1}\mathcal{F}(\mathbf{Q})|^2 \rangle$  with  $V = 8a^3$  and  $Q$  being the  $x$  component of the scattering vector  $\mathbf{Q}$  along [100] and [110], respectively.

We have also analyzed the effect of polydispersity on these calculations, assuming Gaussian size distributions. It is interesting to point out that polydispersity mainly gives rise to a more pronounced smoothing of the  $\ln I$  versus  $\ln Q$  curve. There is also a slight increase in the scale factor, depending on the distribution, which leads to greater values of the particle size. This increase in the scale factor is attributed to the fact that the greatest contribution to the scattering comes from particles outside the distribution center. As a result, the scale factor  $C$  for a monodisperse system is  $C = \frac{1}{6}$ , while  $C = \frac{1}{5}$  is found for systems having Gaussian distributions of full width at half maximum  $\gamma = 0.5\alpha$ , where  $\alpha$  is the cube semiedge of the particle corresponding to the maximum of the Gaussian distribution.

<sup>1</sup>K. Suzuki, J. Phys. Soc. Jpn. **16**, 67 (1961).

<sup>2</sup>K. Toman Czech, J. Phys. B **12**, 542 (1962).

<sup>3</sup>D. Figueroa and E. Laredo, Solid State Commun. **11**, 1209 (1972).

<sup>4</sup>W. Spengler and R. Kaiser, Phys. Status Solidi B **66**, 107 (1974).

<sup>5</sup>A. Guerrero, F. Butler, P. Pratt, and L. Hobbs, Philos. Mag. A **43**, 1359 (1981).

- <sup>6</sup>J. A. Chapman and E. Lilley, *J. Mater. Sci.* **10**, 1154 (1975).
- <sup>7</sup>M. Yacaman, L. Hoobs, and M. Goringe, *Phys. Status Solidi A* **39**, K85 (1977).
- <sup>8</sup>M. Yacaman and R. Vook, in *Proceedings of the 35th Annual Electron Microscopy Society of America*, Boston, 1977, edited by G. W. Bailey (Claitor's Publishing Division, Baton Rouge, 1977).
- <sup>9</sup>C. Cros, L. Hanebali, L. Latié, G. Villeneuve, and W. Gang, *Solid State Ion.* **9&10**, 139 (1983).
- <sup>10</sup>E. Lilley and J. B. Newkirk, *J. Mater. Sci.* **2**, 567 (1967).
- <sup>11</sup>J. M. Calleja, A. Ruiz, F. Flores, V. R. Velasco, and E. Lilley, *J. Phys. Chem. Solids* **41**, 1367 (1980).
- <sup>12</sup>F. Rodríguez, M. Moreno, F. Jaque, and F. J. López, *J. Chem. Phys.* **78**, 73 (1983).
- <sup>13</sup>M. Moreno, J. C. Gómez-Sal, J. Aramburu, F. Rodríguez, J. L. Tholence, and F. Jaque, *Phys. Rev. B* **29**, 4192 (1984).
- <sup>14</sup>J. C. Gómez-Sal, F. Rodríguez, M. Moreno, and J. L. Tholence, *Phys. Rev. B* **37**, 454 (1987).
- <sup>15</sup>J. C. Gómez-Sal, M. Moreno, F. Rodríguez, A. Ravex, and J. L. Tholence, *J. Phys. C* **20**, L421 (1987).
- <sup>16</sup>F. Rodríguez, M. Moreno, J. C. Gómez-Sal, and C. Janot, *Physica B* **156&157**, 33 (1989).
- <sup>17</sup>G. L. Squires, *Introduction to the Theory of Thermal Neutron Scattering* (Cambridge University Press, London, 1978).